Article

Weekly Small Uncrewed Aerial System Surveys, Structure from Motion, and Empirical Orthogonal Function Analyses Reveal Unique Modes of Sediment Exchange Generated by Seasonal and Episodic Phenomena: Waikīkī, Hawai'i

Kristian K. McDonald * , **Charles H. Fletcher, Tiffany R. Anderson and Shellie Habel**

Department of Earth Sciences, School of Ocean and Earth Science and Technology,
University of Hawai'i at Mānoa, Honolulu, HI 96822, USA
* Correspondence: kkmcdona@hawaii.edu

Abstract: Small uncrewed aerial systems (sUASs) provide an efficient way to reveal processes controlling the morphology of sandy shorelines so that they can be more effectively managed. One of Hawai'i's most popular tourist destinations, Waikīkī's Royal Hawaiian Beach, features patterns of sediment transport driven by trade-wind activity, seasonal wave conditions, tropical storm activity, and other phenomena that make it an effective laboratory for the study of beach morphology. To evaluate the efficacy of using consumer-grade sUASs to monitor subaerial sand volume and processes that drive beach morphodynamics, we conducted weekly aerial and ground surveys from which high-resolution point clouds, digital elevation models, and orthomosaics were generated through structure from motion (SfM) photogrammetry. Our period of observation (April to November 2018) bracketed the Central Pacific hurricane season and the season of elevated southerly swell. Both phenomena are known to significantly influence sediment transport in the study area. Using empirical orthogonal function (EOF) analysis, we described combinations of single and dual littoral cell behavior generated by both longshore sediment transport and abrupt episodic fluctuations in cross-shore transport. While past studies have investigated morphological change at this location, this unique single and dual cell behavior within the greater littoral system had not been previously revealed. This study demonstrates that sUASs are capable of capturing high-resolution spatial and temporal topographic data that allow for detailed evaluation of both seasonal processes and abrupt perturbations of beach systems. These processes drive significant changes in beach area, volume, and overall beach morphology and their understanding critical to effective management in an era of sea level rise-driven change. The employed methodology was designed to be highly efficient and universally applicable to sandy shorelines whilst also being relatively inexpensive and instrumentation readily available, allowing for a more comprehensive understanding of these unique coastal environments.

Keywords: small uncrewed aerial systems; sUAS; structure from motion; SfM; sediment transport; beach behavior; beach monitoring; beach morphology; EOF analysis

1. Introduction

Beaches are highly dynamic systems, constantly changing in response to environmental processes, including long-term sea level rise [1]. As many of the world's beaches abut urban and suburban areas, it is necessary to improve understanding of beach behavior on a range of temporal and spatial scales. Waikīkī, located on the southern shore of O'ahu, functions as the premier resort destination of the Hawaiian Islands generating an estimated USD 2.2 billion in visitor expenditure per year [2] while also serving as a cultural and recreational hub for both visitors and residents alike.

Some 70 percent of beaches in Hawai'i are chronically eroding due to both natural and anthropogenic causes [3]. Year-to-year erosion in Waikīkī has required regular intervention to retain sediment and maintain beach area for more than a century [4], and in turn the location has been the subject of multiple scientific studies to inform such projects [5–7]. Until recently, however, traditional beach surveying methods have limited the spatial and temporal resolution of research and thus hampered understanding of more nuanced beach processes. With the advent of consumer-grade small uncrewed aerial systems (sUASs) coupled with modern structure from motion (SfM) photogrammetry software, there is potential to understand beach behavior at a higher level of complexity and detail.

Coastal research using remote sensing platforms has been a rapidly evolving area of study. Early use of remote sensing techniques relied on time series of aerial and/or satellite imagery to determine temporal patterns of shoreline change and remains a useful method [8–14]. The development of Light Detection and Ranging (LiDAR) techniques allowed for the study of three-dimensional subaerial and nearshore coastal variability [15,16], but such methods are often cost prohibitive. High-frequency sampling intervals can be achieved with coastal monitoring stations, such as the ARGUS system [17], but require infrastructure and maintenance and can be subject to high vertical uncertainty [18].

In the mid-2000s, sUASs were more regularly employed in the study of coastal environments owing to their operational flexibility and versatility [19,20]. Lower costs, associated with the growing demand for consumer-grade sUASs, and improved accuracy relative to traditional survey methods [21] have made these platforms practical for studying coastal morphodynamics [22–26]. However, despite the capacity to collect data at higher (e.g., weekly, daily, etc.) temporal resolutions, there are few published studies of beach dynamics using sUASs at these frequencies [27].

Typical coastal monitoring methods have focused on broad-scale beach response and morphological change [16,28,29]. Here, we employ a modified methodology using sUASs that reduces field time when compared to traditional methods, allowing for rapid data collection at approximately weekly intervals. The method produces three-dimensional reconstructions, or point clouds, of the subaerial beach that feature high spatial resolution using SfM analyses. Digital elevation models (DEMs) produced from these point clouds are then compared to gain insight into morphological change during the study period.

DEM time-series analysis is a widely employed method to document morphological change and quantify earth surface processes across a range of time and spatial scales. It is often used to model change in a variety of different environments, from riparian [30,31], volcanic [32,33], and glacial settings [34–37] to earth mineral extraction sites [38–40] and the extraterrestrial [41]. DEMs, or bare-earth raster grids, are referenced to a vertical datum, allowing them to be compared on a cell-by-cell level, often through differencing or other statistical means [42,43].

We conduct empirical orthogonal function (EOF) analyses across the DEM time series and interpret patterns of beach behavior and relationships to environmental data across the period of study. EOF analyses are commonly used across various disciplines to investigate spatial patterns of variability and how they change over time. Such analyses are typically conducted by computing eigenvalues and eigenvectors of a covariance matrix (representing spatial and temporal data that capture elevation change in this case) in which derived eigenvalues provide a measure of percent variance explained by each mode.

The objectives of this study are (1) to identify patterns of morphological variability that have not previously been captured by studies featuring lower temporal and spatial resolution, (2) to interpret patterns of beach change using EOF analysis and identify correlations with long-term and episodic environmental forcing, and (3) to advance understanding of morphodynamics on reef-fronted beaches to inform beach management.

2. Site Description

Royal Hawaiian Beach is a crescent-shaped, carbonate sand beach located in the heart of Waikīkī (Figure 1). The beach's littoral cell extends 520 m and is bounded by

terminal groin structures located at each end that function as artificial headlands and prevent significant longshore transport into or out of the system [7]. Any net sediment gains or losses occur primarily through cross-shore transport [44]; however, pronounced longshore sediment exchange within the cell does create localized erosion and accretion hotspots depending on fluctuations in the wave field [7].
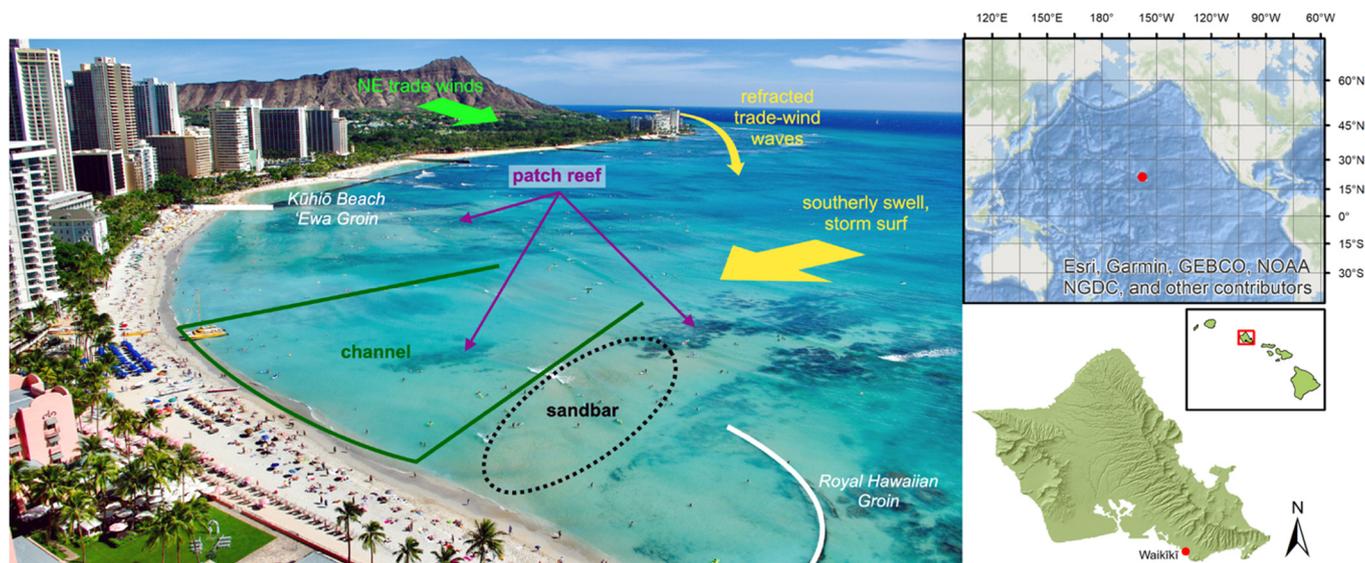

Figure 1. Looking southeast above the Royal Hawaiian Beach. A crescent-shaped, carbonate sand beach located in the heart of Waikīkī on the south shore of Oʻahu. It is a compartmentalized littoral cell, with terminal structures (Kūhiō Groin and Royal Hawaiian Groin) preventing significant longshore transport into or out of the cell. The nearshore is complex, with patch reefs, a shallow submarine channel, and a perennial sandbar adjacent to it. These features interact with wind-generated waves produced by persistent northeasterly trade winds in addition to southerly swell during the summer months and storm surf, typically during hurricane season (June–November).

Sediment in the study area is characterized as moderately well to well-sorted medium sand (D_{50}: 0.29–0.40 mm), with notably coarser grains near the terminal groins (D_{50}: 0.80 mm) [44]. Royal Hawaiian Beach has a long history of sand nourishment. In 2012, the State of Hawaiʻi brought 17,551 m^3 of carbonate sand from a reef-top borrow site located approximately 200 m offshore [7]; a follow-up restoration project was conducted in 2021 following our period of study [45].

The nearshore is characterized by a wide and relatively shallow (1–3 m in depth) carbonate reef platform, an irregular patchwork of fossil reef outcrops separated by mobile and generally thin (<1 m-thick) sand deposits, extending more than 1000 m offshore. The platform is bisected by a shallow submarine sand field occupying a paleo-channel [46]. This sand field acts as a conduit for cross-shore transport, contributing to an average shoreline erosion rate of 0.7 m/year and annual sediment loss of about 1070 m^3 [44]. The complex bathymetry produces complicated wave and current conditions. Previous studies have shown that a wave-induced longshore current typically flows to the northwest (toward the bottom of Figure 1) at velocities generally below 0.15 m/s [47]. However, this current reverses on occasion due to seasonal changes in swell direction [6,47].

Dominant swell regimes for the Hawaiian Islands coincide with the seasons (Figure 2). Southerly swells generated by storms in the southern hemisphere represent the greatest source of wave energy to the study site. These waves are most prevalent between April and October, occurring 53 percent of the time during a typical year [48]. Often traveling more than 8000 km, they have deep-water wave heights ranging from 0.3 to 1.2 m, with periods of 14 to 20 s [44]. Wave direction depends on storm position and track, with resulting swells typically approaching from between the southeast to southwest. Locally generated

waves resulting from trade winds blowing from the east or northeast occur 75 percent of the time during a typical year [48] and are most persistent through summer months [44]. Deep-water wave heights associated with trade-wind waves are typically 0.9 to 2.4 m with periods of 5 to 10 s. The study area, in the lee of the island, is mostly sheltered from this energy, although some trade-wind wave energy is refracted around the southeastern end of the island [44].
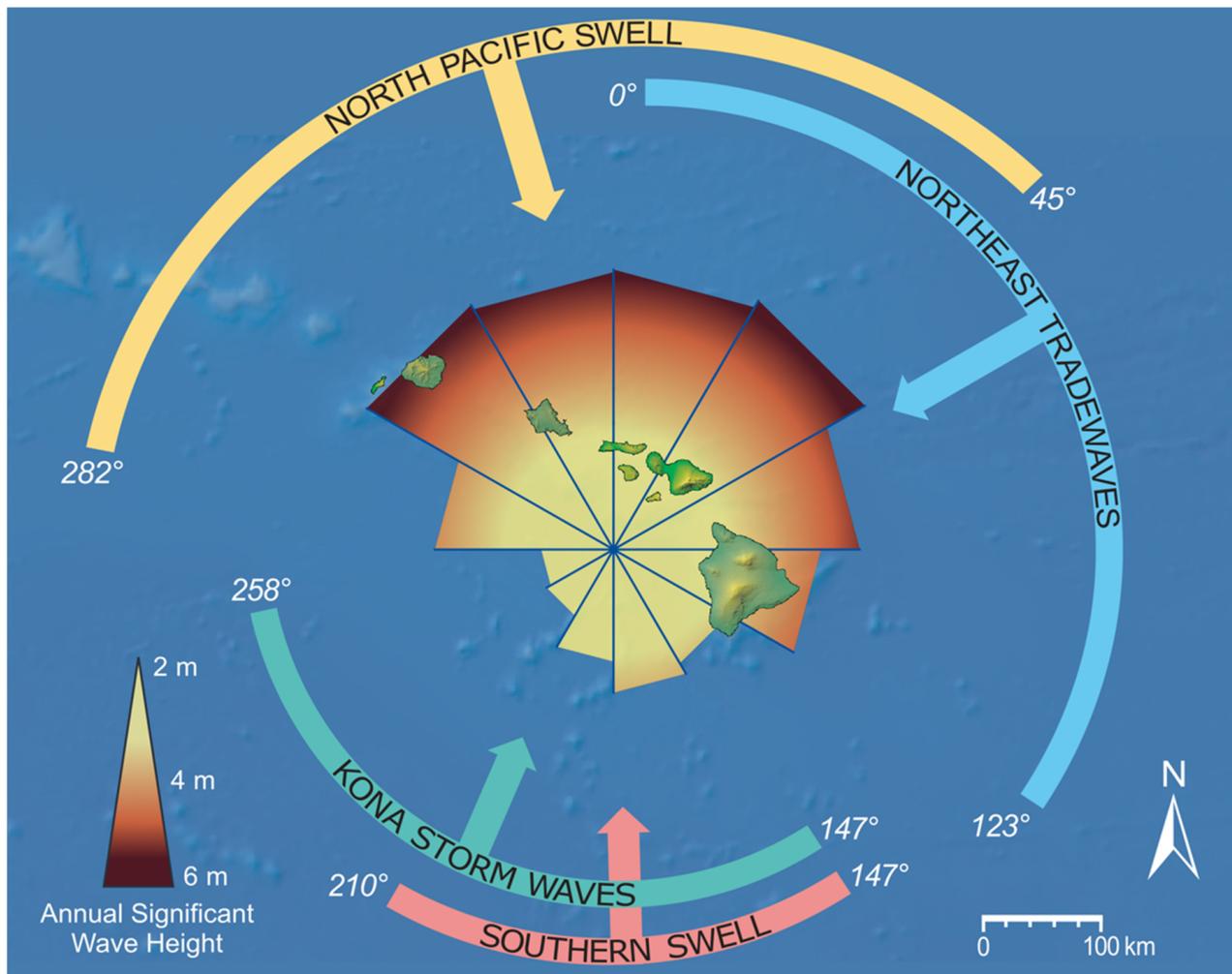
Figure 2. Dominant swell regimes for the Hawaiian Islands. Southerly swell generated by storms in the southern hemisphere represents the greatest source of wave energy to the Royal Hawaiian Beach. Occasionally, storm-generated waves can affect the Waikīkī area via Kona storms or tropical cyclones. Refracted wave energy due to locally generated northeasterly wind-driven waves is also capable of influencing the study site. Northerly swells, typical during the winter season, are mostly blocked by the island and have little influence on the beaches of Waikīkī; however, swells with an extreme westerly or easterly direction may generate some refracted energy into the cell. Adapted with permission from ref. [49], modified after ref. [50]. Copyright 2008 Charles H. Fletcher.

Storm-generated waves and changes in wind direction also affect the Waikīkī area via seasonal extratropical and tropical cyclones. The extratropical cyclones occur near the islands during the Northern Hemisphere cool season as disturbances of extratropical origin propagate towards the equator and spawn disturbances at subtropical latitudes; in the Hawaiian Islands, these disturbances are referred to as Kona storms [51]. Kona storms occur 10 percent of the time during a typical year [48] and are associated with strong southerly and southwesterly winds capable of generating deep-water wave heights of 1 m with larger

waves ranging from 3 to 5 m and periods of 8 to 10 s [47]. Tropical cyclones generally occur near the islands during the Northern Hemisphere warm season as disturbances of tropical origin spawn in the eastern or central Pacific Ocean. Tropical disturbances that travel west into the Central North Pacific basin often pass south of the islands and can produce large surf in the study area. Modeling suggests that potential impacts of global warming on regional cyclone activity include a northwestern shift of regional hurricane tracks such that tropical systems will likely encounter Hawaiian waters more frequently in the future [52].

The 2018 hurricane season was the fourth most active season on record, producing the highest accumulated cyclone energy value in the Central Pacific basin [53]. Four named storms impacted the study site during our monitoring period (Table 1, Figure 3). Hurricane Hector reached Category 4 intensity and passed south of O'ahu in early August, generating deep-water waves that peaked at 1.25 m in height from a south-southwesterly direction (200°–213°). Hurricane Lane occurred at the end of August and attained Category 5 intensity, generating the largest swell of the study period with deep-water heights of just over 2 m from the south-southwest (190°–210°). Hurricane Olivia attained Category 4 intensity and passed just to the south of the study area in mid-September as it weakened into a tropical storm. As it passed, Olivia produced torrential rainfall and tropical-storm-force winds that impacted O'ahu and other islands; however, the event produced only minor swell relative to the other three systems. Hurricane Walaka passed to the south of the study area in late September and early October and attained Category 5 intensity as it tracked to the southwest. This storm produced the second largest swell of the study period with peak deep-water heights just under 2 m from a southwesterly direction (210°–227°).

Table 1. Named storms, the approximate dates at which they influenced the study site (according to wind and wave data), peak intensity (Saffir–Simpson Hurricane Wind Scale) along with 1-min maximum sustained wind speed at peak intensity [54–57]. Tropical Storm Olivia attained Category 4 intensity but weakened to a tropical storm prior to its influence on the Hawaiian Islands, as depicted in Figure 3.

Tropical Cyclone	Dates of Influence	Peak Intensity
Hurricane Hector	9 August 2018–15 August 2018	Category 4, 250 km/h
Hurricane Lane	20 August 2018–27 August 2018	Category 5, 259 km/h
Tropical Storm Olivia	10 September 2018–14 September 2018	Category 4, 213 km/h
Hurricane Walaka	2 October 2018–6 October 2018	Category 5, 259 km/h

Northerly swells, generated by winter storms in the northern hemisphere, produce deep-water wave heights as great as 9 m at periods of 12 to 20 s [44] but are mostly blocked by the island and have little influence on the beaches of Waikīkī. Swells with an extreme angle of approach, however, may generate some refracted energy into the area.
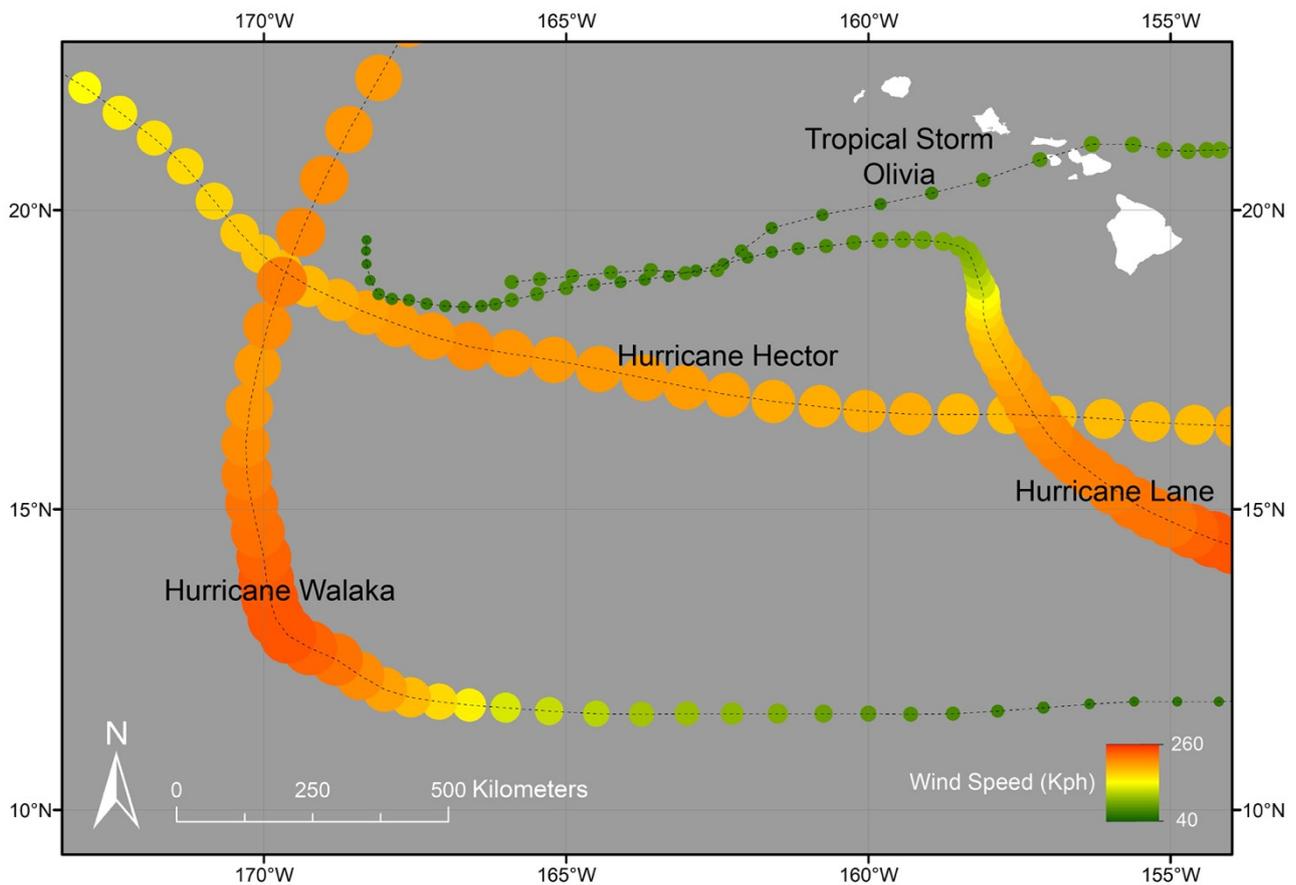
Figure 3. Tropical cyclone activity during the 2018 Central Pacific Hurricane Season, which included four named storm systems that directly impacted the study area. Wind speeds along each storm track are symbolized according to point size and color [58,59].

The subject beach is known to experience erosion under shorter-period winter waves associated with the trade winds and accretion under longer-period southerly swell in the summer [6,7,60]. In a study of beach behavior following the 2012 nourishment project, it was found that seasonal changes in the wave field caused the beach volume to fluctuate by 2000–4000 m^3 (15 percent to 30 percent of total nourishment addition) over the course of 2.7 years [7]. Beach volume decreased at a rate of 760 $\pm$ 450 m^3/year, totaling less than that influenced by observed seasonal adjustments. Additionally, they observed a long-term east-to-west transport accompanied by cross-shore transport, with nearshore sand fields acting as both a sand source (during storm-related swell events) and sink (during non-storm periods) depending on seasonal conditions. A study of Royal Hawaiian Beach used aerial surveying and image classification methods to track changes in beach morphology [27] and found that water level variability and wave energy flux were the primary drivers of beach change through a combination of longshore and cross-shore sediment exchange.

3. Methodology

3.1. Surveying

We conducted a weekly monitoring program from mid-April to the end of November of 2018 using consumer-grade sUASs, capturing the effects of both seasonal and tropical-storm-generated waves. The initial survey was conducted about one week prior to the first significant southerly swell of the summer season to establish a baseline beach state, with 26 subsequent weekly surveys thereafter.

Aerial surveys were conducted using a Phantom 4 Pro V2, a consumer-grade quadrotor sUAS manufactured by DJI. This sUAS was chosen due to its availability and ease of use,

relatively long flight time (~30 min), stock 3-axis gimbal with a 20-megapixel red-green-blue (RGB) sensor, and compatibility with 3rd-party flight planning software. Additionally, the sensor utilizes a global shutter, meaning that all pixels of the image sensor array are exposed simultaneously, enabling the capture of moving targets without the spatial distortion that can be experienced from rolling shutters of previous Phantom model sensors. This results in improved accuracy and reduced image processing times [61].

Flights were semi-automated using the flight planning software package DroneDeploy that collected still imagery with 80 percent overlap in both x and y. Flight height was set at 120 m above launch elevation, allowing clearance of buildings and other structures while optimizing image resolution and maintaining Federal Aviation Administration (FAA) airspace compliance. Owing to small variations in beach elevation of less than 4 m, the ground sample distance remained between 115 m and 120 m for all surveys. Camera parameters were dependent on conditions and lighting, but high shutter speeds (1/1000–1/600) were used to reduce motion blur of objects and distortion introduced by the movement of the image collection system.

Seven 1×1 m vinyl targets were placed at approximately equidistant intervals along the length of the subaerial beach and functioned as ground control for each aerial survey. Ground control points were surveyed in the field using a rod-mounted prism and a Leica TS16 Robotic Total Station. Surveying was accomplished early in the day to avoid the hours of heavy public use; thus, conditions were random with respect to wave state and tide cycle. Existing benchmarks were used to orient the spatial reference using the WGS 1984 UTM Zone 4 projection. Elevations were measured with respect to local mean sea level (LMSL) [62].

3.2. Three-Dimensional Beach Reconstruction

Point clouds and orthomosaics were produced using Photoscan (now Metashape), a photogrammetric processing application developed by Agisoft LLC. The process generally follows a methodology developed by the United States Geological Society [63] in which imagery taken by sUASs is combined with surveyed control points in an iterative process to reduce errors and produce map-quality three-dimensional surface reconstructions. Points in the sparse point cloud model generated via the initial photo alignment are assigned uncertainty values, namely reconstruction uncertainty, projection accuracy, and reprojection error, by the software. Points above a designated threshold were removed after which the point cloud was realigned. This process was repeated until the error values were at or below the designated threshold. The dense point clouds produced from the best available points as determined through this process were then exported for additional processing using Rapidlasso's LAStools, a software suite allowing for batch-scriptable, multi-core processing of point cloud data. The automated LAStools processing involved standard remotely sensed data processing (e.g., masking, thinning, and classifying) of the point cloud in addition to the removal of stationary objects along the beach (e.g., beach umbrellas and canoes) and noise introduced at the foreshore due to saturated sand and wave run-up. Manual assessment and removal of any residual noise were conducted for each post-processed point cloud.

Post-processed point clouds were imported into ESRI's ArcMap, following which DEMs with 0.5 m resolutions were generated using natural neighbor interpolation. The DEMs were smoothed using mean cell values located within a 5 m radius circular neighborhood to reduce noise and to reveal larger-scale patterns of variability. The DEM time series was used for all analyses including width, volume, surface area, surface variability, and empirical orthogonal function (EOF) analysis.

3.3. Beach Width, Volume, and Surface Area

Beach width, volume, and surface area were calculated for the subaerial (dry) beach above the mean higher high water (MHHW) tidal elevation. MHHW, which is measured at 0.329 m above LMSL at the nearby Honolulu tide gauge [62], is used to represent an upper

bound of present-day sea level in coastal studies of the urban corridor of O'ahu [64]. Beach width, calculated at 5 m intervals along the beach (totaling 98 transects), was defined as the distance between the seaward edge of the beach (where the beach surface intersects the MHHW elevation) and the inland edge of the beach (typically identified by cement walkways or other engineered structures). Volume and surface area were calculated relative to MHHW using the ArcGIS tool "Surface Volume".

3.4. Uncertainty

To quantify error in the sUAS-derived DEMs, a separate survey was conducted, in which a total of 228 elevation measurements were taken randomly throughout the study area using a Leica TS16 Robotic Total Station, which results in mm-level accuracy. Simultaneously, sUAS imagery and ground control points were collected, from which a DEM was created following the methods presented in this study.

Errors in DEM elevations were calculated by taking the measured total station elevations, assumed as accurate, and subtracting from them from the respective DEM elevations representing the same location. The mean of the discrepancies between the total station elevations and the model was effectively zero (0.006 m), and measured locations were sufficiently spaced such that there were no observed spatial correlations between adjacent error values. Thus, the measured errors are considered to be randomly distributed about a mean of zero, and the standard deviation of the mean of errors,

$$\sigma_\mu = \frac{\sigma}{\sqrt{n}} ,\tag{1}$$

was used in the uncertainty calculations and determined to be 0.007 m, where σ is the standard deviation of the errors themselves (0.1 m, RMSE = 0.1 m), and n is the number of total station elevation measurements.

From these randomly distributed errors, the uncertainty in beach width and surface area was quantified by determining the upper and lower bounds of the beach. The smaller bound represented the width and surface area of the beach whose seaward edge intersected the MHHW + σ_μ elevation contour; the width and surface area of the beach whose seaward edge intersected the MHHW − σ_μ constituted the larger bound. Beach width and surface area uncertainty were then calculated as one-half the distance/difference in area representing the smaller and larger bound, respectively.

The uncertainty in sediment volume from each DEM is estimated as

$$U_{vol_j} = A_j \sigma_\mu \tag{2}$$

where A_j is the footprint, or area, of the jth sUAV-derived DEM of the subaerial beach, and σ_μ is the standard deviation of the mean of errors, as described above.

3.5. Empirical Orthogonal Function Analysis

Empirical orthogonal function (EOF) analysis was used to quantify spatiotemporal modes of variability of the subaerial beach. EOF analysis is a common method of multivariate analysis that is highly useful in revealing dominant modes of variability within datasets, such as those that capture beach profile evolution [7,60,65–69]. As is standard in EOF analysis, the time average was removed in order to describe variations from the mean beach. Our analysis focuses on the first three modes of variability which represent 74 percent of the total data variance.

3.6. Shoreline Response to Wave Forcing

Beach volume and surface area calculations, DEM surfaces, and EOF modes of variability were compared to regional wave and wind conditions to determine morphological response of the beach. Data describing local wave and wind conditions are hosted by PacIOOS (www.pacioos.org, accessed on 3 December 2018), which is part of the U.S. In-

tegrated Ocean Observing System, funded in part by National Oceanic and Atmospheric Administration (NOAA). Data sourced from PacIOOS are described hereafter. Regional hourly modeled significant wave height, mean direction, and mean period were acquired from the Simulating Waves Nearshore (SWAN) Regional Wave Model for the island of O'ahu (Figure 4a–c). The high-resolution (500 m) SWAN model simulates shallow water effects and nearshore coastal dynamics with a 7-day output [70]. Regional hourly wind speed and direction were obtained from the Weather Research and Forecasting (WRF) model, a 1.5 km resolution open-source numerical weather prediction system (Figure 4d,e). The data were obtained for the grid cell most proximate to the study area (21.27°N, 157.827°W). A proxy for wave energy flux generated by southern hemisphere swell (wave periods: 14–30 s; wave direction: 147–220°N) and locally generated trade-wind waves (wave periods: 3–10 s; wave direction: 45–160°N) were calculated following Mikkelsen et al. (2022) [27] in which spectral measurements were obtained from offshore buoys [71,72], and energy density of the relevant frequencies and directional bins of the wave spectrum was multiplied with peak wave period [27] (Figure 5b,c).
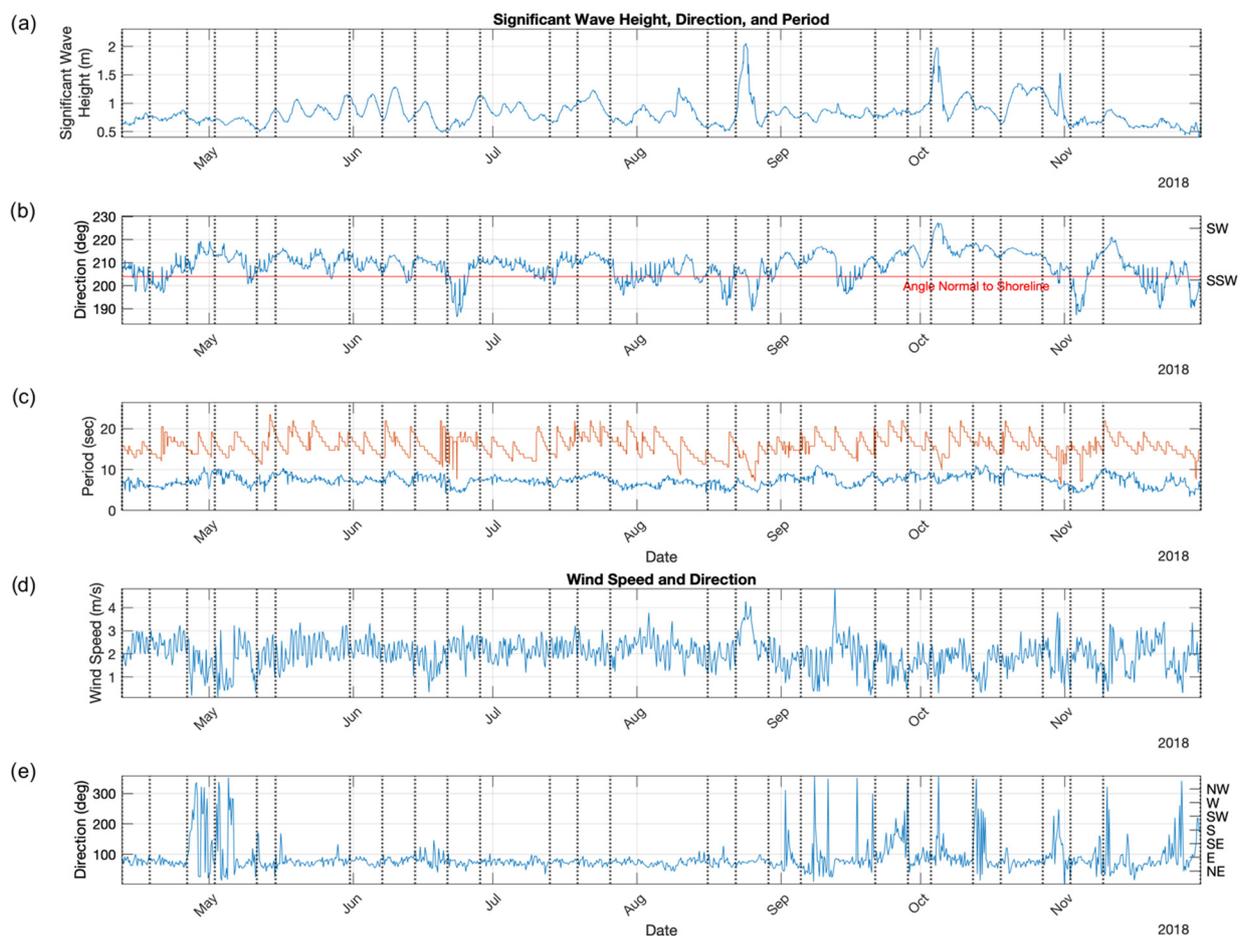
Figure 4. Wave (height, direction, and period; (**a**–**c**)) and wind (direction and speed; (**d**,**e**)) conditions for the study period. Wave and wind data were obtained from PacIOOS model output for the nearest grid cell proximal to the study area following Habel et al. (2016) [6]. Days on which surveys were conducted are delineated by dotted vertical lines.

Figure 5. Surface area and volume of the subaerial beach above MHHW (**a**) plotted alongside incident wave energy flux for south swell ((**b**); wave periods: 14–30 s; wave direction: 147–220°N) and wind flux for trade winds ((**c**); wave periods: 3–10 s; wave direction: 45–160°N). A gradual increase in area and volume throughout the time series: the beach gained 708.5 ± 43.5 m^2 (area) and 1384.8 ± 102.2 m^3 (volume). The overall trend of accretion was interrupted by short-lived erosion events, following which the overall accretion continued. Losses in area and volume coincide with increases in trade-wind energy flux above a threshold of approximately 1×10^5 W/m^2. Gains in area and volume coincide with south swell energy flux above a threshold of approximately 1.5×10^4 W/m^2.

4. Results

4.1. Variation in Beach Width

To identify variations in beach width over the study period, the mean widths of the 98 transects were removed from corresponding beach width measurements and plotted with respect to survey date and transect location (Figure 6). It was found that transect widths fluctuated throughout the study period, varying from respective means by as much as 3.5 m (Figure 7). Most transects from surveys conducted early in the time series (April–June) were narrower than their respective means, particularly at the western end (transects 1 to 30) and just east of the central region (transects 55 to 85) of the study area; however, widths were slightly wider than their respective means just to the east of each of these regions. The width patterns indicate beach behavior acting as two separate littoral subcells during this time period, in which dual cell activity corresponds with periods of

low south swell known to occur during the winter months. This concept of independent subcells is also described in the analysis of the EOF outputs (Section 4.3). Drivers of such behavior are explored in the discussion (Section 5).
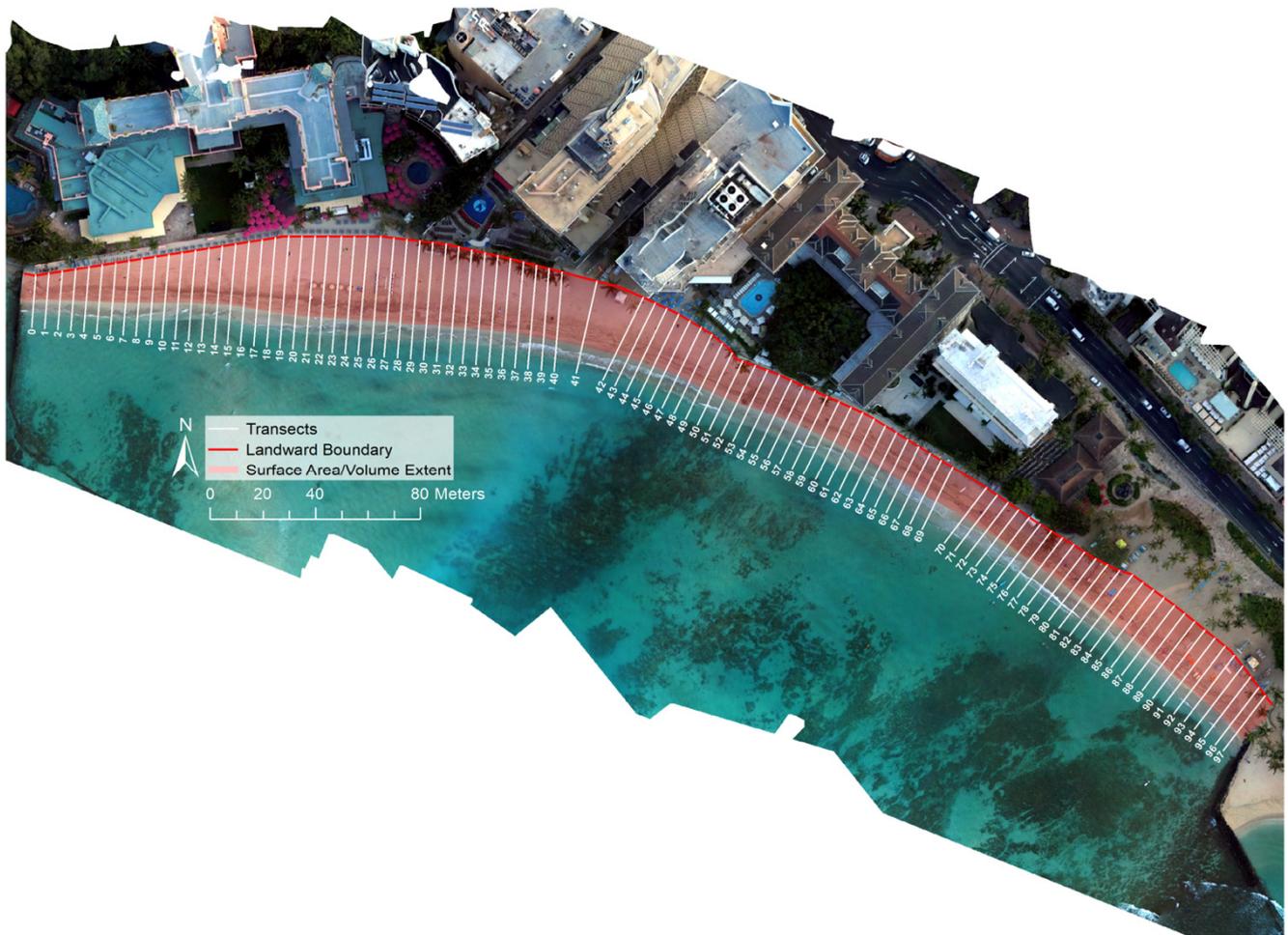
Figure 6. To determine beach width, transects were cast at 5-m intervals along the beach. Beach width was defined as the distance between the seaward edge of the beach (where the beach surface intersects the MHHW elevation) and the inland edge of the beach (typically identified by cement walkways or other engineered structures) and calculated for each transect. The above figure represents transect IDs for the study area. For reference, Transect 0 is located at the west end of the study area adjacent to Royal Hawaiian Groin, while Transect 97 is at the east end adjacent to Kūhiō Groin. The transparent overlay represents the extent of the beach above MHHW used for beach width, surface area, and volume calculations. Orthomosaic basemap generated from the 15 May 2018 aerial survey.

Fluctuation between dual cell and single cell activity occurred from the beginning of June until the beginning of August, following which single cell behavior predominated until mid-October, corresponding to periods of elevated seasonal south swell and tropical-storm-induced swell. The single cell behavior is demonstrated by erosive/accretive hot spots located at the easternmost and westernmost ends, respectively. The abrupt beginning of clear single cell behavior coincides with passage of Hurricane Hector, the first hurricane of the season to pass the study area, and ends following passage of Hurricane Walaka, the season's final hurricane to pass the study area. Following strong trade-wind activity affiliated with Tropical Storm Olivia, transects 25 to 70 experienced abrupt increases in erosion and associated accretion along transects 1 to 24. Similar erosion activity specifically along transects 25 to 45 occurred following strong trade-wind activity in late November indicating potential for strong trade-wind activity to cause erosion specifically in this

section of the beach and associated accretion to the west from transects 1 to 24. Each of these events featured trade-wind energy flux exceeding 1.5×10^5 W/m^2 (Figure 5c).
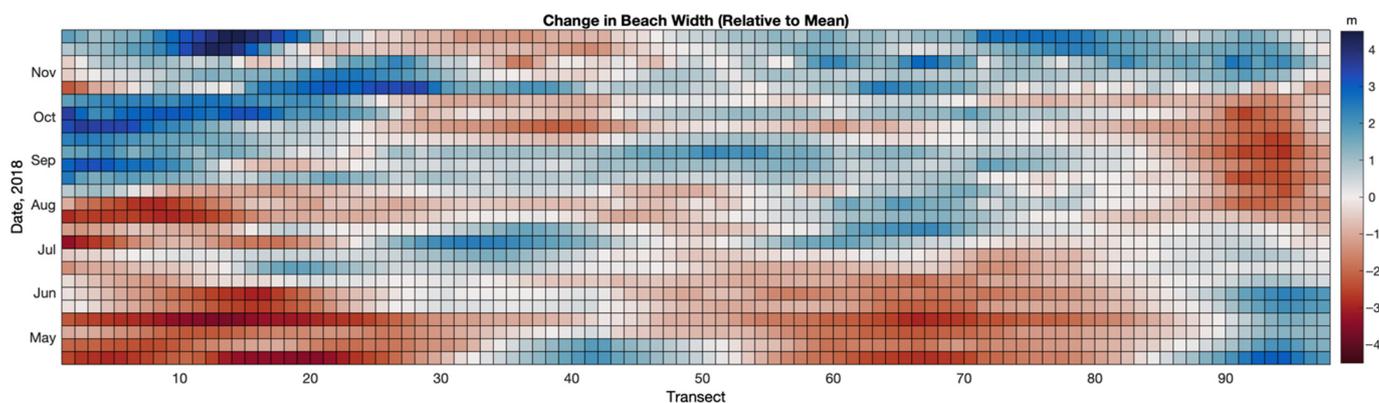
Figure 7. The above figure represents differences from mean beach width for each transect across the DEM time series. Each grid cell corresponds to one transect (x-axis) on a particular survey date (y-axis), while the colors correspond to widths narrower than the mean (red) and widths wider than the mean (blue). The first survey is represented by the bottom row, and subsequent surveys are represented by each row above thereafter. For spatial reference with Figure 1, Transect 0 is represented by the leftmost column. Most transects early in the time series were narrower than their means, but this pattern gradually shifted during the second half of the survey period as beach width increased.

### 4.2. Changes in Surface Area and Volume

To gain additional perspective on forcing related to wind and wave characteristics, we examined changes in subaerial beach area and volume over the monitoring period relative to the initial survey (Figures 4 and 5). Overall, we found a gradual increase in area and volume throughout the time series: the beach gained 708.5 ± 43.5 m^2 (area) and 1384.8 ± 102.2 m^3 (volume). This trend was not unexpected as the period of study aligned with seasons of known accretion previously observed within the study area [7]. The overall trend of accretion was interrupted by short-lived erosion events, following which the overall accretion continued. The rate of recovery differed after each erosion event, but recovery within 1–3 weeks was typical. As the beach accreted and eroded, the surface area and volume trends were approximately consistent with respect to each other, particularly during the first half of the study period. During the second half of the study period, more pronounced increases and decreases in surface area led to a slight relative decoupling of the trends between the two metrics, which may be related to variations in beach slope.

Relationships between forcing (wind and wave conditions) and beach response are evident when comparing metrics of area and volume change to variations in south swell and trade-wind energy flux (Figure 5b,c). Losses in area and volume coincide with increases in trade-wind energy flux above a threshold of approximately 1×10^5 W/m^2; five events illustrate this relationship (late April, early July, early to mid-September, late October, and mid-November). Gains in area and volume coincide with south swell energy flux above a threshold of approximately 1.5×10^4 W/m^2 in which four events illustrate this relationship (mid-May through late June, mid-August, late August, and early October). Increases in south swell energy flux during the study period were generated by seasonal south swell events and by locally generated hurricane swells apart from Tropical Storm Olivia, which, unlike the other three storm events, did not produce swell and instead led to increased wind speeds exceeding 4 m per second. Volume gains were especially notable during periods in which south swell energy flux above the identified threshold coincided with periods of trade-wind energy flux of less than 0.25×10^5 W/m^2; however, when wave energy flux exceeding the given threshold coincided with trade-wind energy flux exceeding 1×10^5 W/m^2, losses in surface area and volume occurred as observed during early July. These findings are consistent with those of Mikkelsen et al. (2022) [27]

that identified correlations between erosional events and peaks in trade-wind swell and correlations between accretional events and increases in south swell energy flux.

4.3. Empirical Orthogonal Function Analysis

Figure 8a–f depicts the results of EOF analysis including three principal spatial modes and their respective temporal components. Together, the three modes represent 74 percent of the topographic variability observed throughout the monitoring period. We interpret vertical changes in beach topography as inflation (accretion, blue) and deflation (erosion, red) when coupled with a positive temporal coefficient, and the opposite (erosion, blue; accretion, red) when coupled with a negative temporal coefficient.
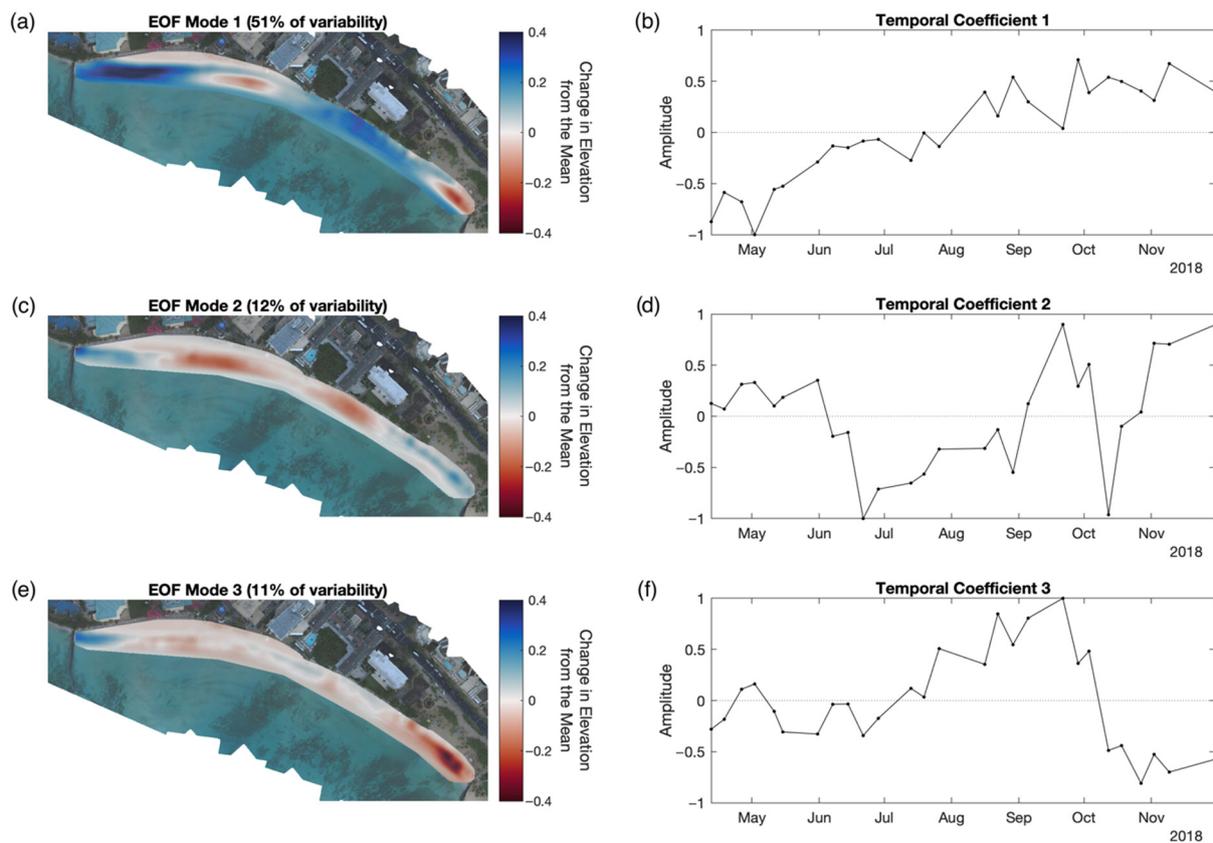
Figure 8. The first three spatial modes (**a**,**c**,**e**) and their respective temporal coefficients (**b**,**d**,**f**) of the EOF analysis, representing 74 percent of the variability of the study area during the study period. We interpret vertical changes in beach topography as inflation (accretion, blue) and deflation (erosion, red) when coupled with a positive temporal coefficient (above the dotted line), and the opposite (erosion, blue; accretion, red) when coupled with a negative temporal coefficient (below the dotted line).

The first spatial mode (Figure 8a) represents 51 percent of the topographic variability observed throughout the monitoring period. The mode reveals two distinct regions with similar patterns of erosion/accretion located along the eastern and western sectors of the study area, respectively. We interpret these as distinct littoral "subcells", which demonstrate nearly identical patterns of behavior. The adjacent positions of eroding and accreting sections within each subcell suggest that eroding portions may be acting as sand sources to the accreting portions, likely driven by longshore littoral transport known to occur within the study area [6,7]. The overall westward rotation of both subcells, as illustrated by the spatial mode and overall positive trending temporal coefficient (Figure 8b), tends to coincide with mild trade-wind energy flux below approximately 1×10^5 W/m^2 threshold, in which deviations in the temporal coefficient coincide with trade-wind energy flux above this threshold. Specifically, such deviations occur in early May, early July, early to mid-

September, late October, and mid-November of 2018. In each case, deviations correspond to losses in beach area and volume and correspond to positive trends in temporal coefficients of EOF modes 2 and 3, which suggests that distinct changes in behavior occur when this threshold in trade-wind energy flux is exceeded.

The second EOF mode (Figure 8c,d) represents 12 percent of the topographic variability observed throughout the monitoring period. Like the first spatial mode, two subcells are apparent. However, unlike the behavior of EOF mode 1, the sediment transport patterns revealed in the second spatial mode mirror rather than mimic each other. Here again, the two subcells share a boundary near the center of the study area in which the positive and negative representations of the mode respectively represent inflation/deflation of the central section of the beach and deflation/inflation adjacent to the artificial headlands (i.e., groins). The temporal coefficient of mode 2 (Figure 8d) is punctuated by abrupt negative trends that coincide with periods of increased south swell wave energy flux and by abrupt positive trends that coincide with periods of increased trade-wind energy flux. Negative trends correspond to events including extended large south swell that occurred during the first half of June and as part of elevated swell generated by Hurricanes Hector, Lane, and Walaka. Positive trends occurred corresponding to elevated periods of trade-wind energy flux generated by Tropical Storm Olivia and during periods of elevated trade winds in late October and November.

Representing 11 percent of the total variability, we interpret the third spatial mode (Figure 8e) as representing one single cell spanning the greater littoral system. The coupled spatial and temporal pattern (Figure 8f) illustrates overall westward rotation during periods in which trade-wind energy flux exceeds an approximate threshold of 1×10^5 W/m^2 and/or when wave energy flux increases in combination with a wave approach that is near normal to or relatively east of normal to the shoreline orientation. Reversals in rotation tend to occur as south swell wave energy flux increases in combination with wave approach that is relatively west of normal to the shoreline orientation. An example of such reversal occurred in response to swell originating from an SSW direction generated by Hurricane Walaka, which resulted in a reversal in sand transport direction from west to east.

5. Discussion

Previous studies of Royal Hawaiian Beach [6,7,47] that employed data of coarser spatial and temporal resolution concluded that the beach operated mainly as a single littoral cell. It was found that the predominant behavior could be described by reversals in transport direction driven by seasonal changes in wave energy and direction. It was also found by these studies that the beach generally features erosion during the winter season along with sediment transport to the east and accretion during the summer season along with sediment transport to the west coinciding with the onset of southerly swells [5,6]. Similar to the present study, Habel et al. (2016) [7] employed EOF analysis to identify the described sediment transport patterns. However, their methods consisted of traditional elevation surveys conducted quarterly during their study period, representing topographic data of lower temporal and spatial resolution relative to the present study. While Habel et al. (2016) [7] were able to establish overarching patterns of seasonal sediment transport, the investigation was limited in its ability to analyze behavior coinciding with more specific wind and wave regimes. Further, the behavior revealed by primary EOF modes was dominated by the 2012 beach nourishment event and subsequent equilibration that the study was designed to monitor and thus did not capture the relatively subtle naturally driven behavior of the littoral cell.

The use of EOF analysis in combination with higher resolution data and the absence of large beach management projects such as the 2012 nourishment revealed subtle modes of beach behavior that highlight more complex patterns of sediment exchange. These consist of combinations of single and dual cell activity that drive the overall morphodynamics of the study area. Overall, the predominant behavior over the surveyed time period has been revealed as dual cell rotation to the west according to the principle EOF mode (Figure 8a).

This mode accounts for approximately half the topographic variability observed and features an overall positive trend in the temporal coefficient (Figure 8b). Further, transport direction and approximate alignment with the prevailing ENE trade-wind regime suggest that the behavior is generated by mild ENE trade winds and in turn trade-wind energy flux that contributes to the dual cell longshore transport processes. Genesis of the dual cell activity and basis for the location of their division remain unclear; however, these may be related to the disruption in longshore activity due to cross-shore currents related to the non-linear shoreline orientation and/or presence of a centrally located offshore channel, as described in Section 5.2.

5.1. Trade-Wind-Driven Transition from Dual Cell to Single Cell Behavior and Generation of Cross-Shore Transport Patterns

Increases in ENE trade-wind speed, and in turn trade-wind flux above the threshold of approximately 1×10^5 W/m^2, shift beach behavior from dual cell westward rotation to single cell westward rotation as indicated by reversals in the temporal coefficient of EOF mode 1 (Figure 8b) and corresponding positive trends in the temporal coefficient of EOF mode 3 (Figure 8f). This suggests that as winds exceed the stated threshold, centrally located disruptions in longshore transport are overcome, initiating single cell transport behavior.

Increases in trade-wind energy flux above the stated threshold also correspond to losses in overall beach area and volume and positive trends in the temporal coefficient of EOF mode 2 (Figure 8d), suggesting generation of cross-shore sediment transport in the offshore direction. For example, two episodes of increased trade-wind energy flux, one in late May and the other generated by Tropical Storm Olivia in mid-September, correspond to relatively large erosion events and increasing trends in the temporal coefficients of EOF modes 2 and 3. In late May, 964.2 ± 97.5 m^3 of sediment were eroded, and in September, 1233.0 ± 103.7 m^3 were lost. These findings reinforce and explain the Mikkelsen et al. (2022) [27] finding that high windspeed trade winds drive accelerated erosion on the eastern beach extent and reduced accretion on the western beach end, as well as the finding that strong wind speeds alter predominant longshore and cross-shore currents.

While erosion tended to be influenced by increases in trade-wind energy flux, accretion appeared to be driven by increases in south swell energy flux. The presence of hurricane-related swell coincides with increases in overall surface area over relatively short time periods. From the beginning of August to mid-October, three named storm events (Hurricanes Hector, Lane, and Walaka) produced sizable swell that coincided with approximately doubled surface area of the overall beach from ~400 m^2 to ~900 m^2 across the respective time period. These increases in area and volume correspond with negative shifts in EOF mode 2, suggesting the influence of cross-shore sediment transport in the onshore direction as wave energy flux exceeded 2.5×10^4 W/m^2. These findings identify south swell wave energy flux approximately exceeding this threshold as the driver of cross-shore transport in the onshore direction, answering a question left unconfirmed by Habel et al. (2016) [7] which speculated that increases in beach volume coincide with increased incident wave energy flux during the summer months. While the reasons for this phenomenon require further study, we hypothesize that sediment eroded from the beach during the winter months settles in the centrally located offshore channel. As south swells influence the area during summer months, particularly those that exceed the wave energy flux as described above, waves propagate through the channel creating the cross-shore currents in the onshore direction, leading to sediment deposition along the beach and increases in surface area and volume. A more detailed discussion regarding the formation of these currents can be found in the following section.

5.2. Alternating Rip-Current Formation

Topographic gains along the central beach extent and moderate losses near the terminal structures, as indicated by the spatial component of EOF mode 2 (Figure 8c), suggest the formation of rip currents as wave energy travels landward through the centrally

located offshore channel and returns seaward near the eastern and westernmost terminal structures. Such rip currents are known to form in the center of embayments and adjacent to headlands [73] both of which are featured in the study area. Cross-shore sediment transport is suggested by patterns of topographic loss in the central section of beach that correspond to increases in trade-wind energy flux and overall beach volume/area loss. Cross-shore transport is also suggested by patterns of topographic gains in the same area that correspond to increases in south swell energy flux and overall beach volume/area gain. Abrupt variations in the temporal component of EOF mode 2 (Figure 8d) in which positive trends correspond to increases in trade-wind energy flux and negative trends correspond to increases in south swell energy flux suggest that rip currents form at the center of the embayment during elevated periods of trade-wind energy flux and adjacent to artificial headlands (i.e., groins) during elevated periods of south swell. Topographic gains in areas opposite to those experiencing loss may suggest the presence of feeder currents running adjacent to rip currents, causing accretion landward of those areas.

South swell energy flux in the form of large-wave-inducing far-field storms and hurricanes and trade-wind energy flux in the form of a wind-inducing near-field tropical storm provide extreme examples of how episodic wave and wind events likely generate cross-shore sediment transport in both onshore and offshore directions within the study area. Such information regarding rip-current generation and location is useful to decision makers overseeing beach use and safety. Past studies have verified that (1) currents move through the centrally located channel, which acts as a conduit through which cross-shore sediment transport occurs, and (2) that currents have been observed in this channel featuring velocities of over 0.9 m/s [47]. Novel to this study is the recognition that cross-shore current reversals (i.e., rip-current formation and location) likely occur in accordance with relatively predictable wind- and wave-generated swell.

5.3. South Swell Energy Flux an Additional Driver of Single Cell Behavior

As mentioned above, the transition from single to dual cell behavior occurs as trade-wind energy flux surpasses approximately 1×10^5 W/m^2 as indicated by EOF spatial and temporal components 1 and 3 (Figure 8a,b,e,f). The transition also coincides with south swell events beginning in early June and continuing through the beginning of October during which south swell energy flux exceeds 1×10^4 W/m^2. While south swell events and associated volume and surface area gains continue until approximately late October to early November, the clear single cell western rotation appears to reverse with the passage of Hurricane Walaka, which produced large swell from the southwest, and relatively west of normal to the beach profile angle. This direction of wave approach represents the westernmost swell direction of the entire study period and likely explains why the direction of rotation reverses as indicated by an abrupt negative trend in the temporal coefficient of EOF mode 3. The unusual wave approach also explains erosional/accretional width change patterns at the far western/eastern extents of the beach, respectively following passage of the hurricane.

Finally, topographic patterns of variability illustrated by EOF 3 do not clearly coincide with changes in volume and surface area but instead indicate initiation and reversals in single cell longshore transport behavior. This finding further reinforces the hypothesis that the mode mainly characterizes longshore sediment transport behavior owing to the presence of terminal structures at each end of the study area that block gains and/or losses that may otherwise occur as a result of movement of sediment between adjacent littoral cells.

6. Conclusions

Results from weekly survey data collected between April and November of 2018, combined with SfM and EOF analyses illustrate the efficacy of methods that employ low-cost, consumer-grade sUASs to conduct high-frequency coastal monitoring. Such methods are highly effective towards developing a detailed understanding of predominant drivers

that influence coastal morphology. These findings are especially useful given the site-specific conditions that influence carbonate beaches due to the complex bathymetry of fringing reefs in environments that experience tropical storm systems and other seasonal and/or episodic phenomena.

Previous studies of Royal Hawaiian Beach [6,7,47], which employed data with coarser spatial and temporal resolution, concluded that the beach operated mainly as a single cell that featured seasonal reversals in transport direction. The unique contribution of this study is the higher spatial and temporal resolution of topographic data and prevalence of large-scale perturbations of the system (i.e., tropical cyclones), which has allowed a more thorough evaluation of natural drivers that influence transport patterns affecting erosion/accretion, beach morphology, and rip-current formation.

Specifically, the study revealed the presence of three dominant and highly unique transport patterns driven by mild trade-wind energy flux (EOF 1), large episodic perturbations in trade-wind energy flux and south-swell energy flux generated by episodic phenomena such as tropical cyclones (EOF 2), and reversals in larger-scale sediment transport patterns driven by variations in swell direction, south swell energy flux, and increases in trade-wind energy flux (EOF 3). We also showed that high spatial and temporal resolution monitoring of carbonate beaches, which are underrepresented in the global literature, can be performed in an affordable way and yield insights to their behavior that can inform management decisions. This is critical given their high economic value in the global tourism economy.

These data will assist managers, engineers, and other stakeholders in developing strategies to sustain Royal Hawaiian Beach. Considering the economic, ecological, recreational, and cultural value of carbonate beaches, we see these techniques as globally applicable. Given the likely continuation and acceleration of global mean sea level rise, many levels of stakeholders are invested in sustaining these high-value beaches for as long as possible. For these reasons, affordable, high-resolution systems, such as consumer-grade sUASs used in tandem with SfM and EOF analyses, prove to be a valuable tool for the management of coastal areas.

References

1. Jackson, D.W.T.; Short, A.D. 1—Introduction to Beach Morphodynamics. In *Sandy Beach Morphodynamics*; Jackson, D.W.T., Short, A.D., Eds.; Elsevier: Amsterdam, The Netherlands, 2020; pp. 1–14. ISBN 978-0-08-102927-5.
2. Tarui, N.; Peng, M.; Eversole, D. Economic Impact Analysis of the Potential Erosion of Waikīkī Beach. 2018. Available online: https://seagrant.soest.hawaii.edu/wp-content/uploads/2018/08/Economic-Impact-Analysis-Waikiki-Beach-1016-web.pdf (accessed on 1 August 2022).

3. Fletcher, C.H.; Romine, B.M.; Genz, A.S.; Barbee, M.M.; Dyer, M.; Anderson, T.R.; Lim, S.C.; Vitousek, S.; Bochicchio, C.; Richmond, B.M. *National Assessment of Shoreline Change: Historical Shoreline Change in the Hawaiian Islands*; US Department of the Interior, US Geological Survey: Reston, VA, USA, 2012.

4. Wiegel, R.L. Waikiki Beach, Oahu, Hawaii: History of Its Transformation from a Natural to an Urban Shore. *Shore Beach* **2008**, *76*, 3.

5. Wang, N.; Gerritsen, F. Nearshore Circulation and Dredged Material Transport at Waikīkī Beach. *Coast. Eng.* **1995**, *24*, 315–341. [CrossRef]

6. Miller, T.L.; Fletcher, C.H. Waikīkī: Historical Analysis of an Engineered Shoreline. *J. Coast. Res.* **2003**, *19*, 1026–1043.

7. Habel, S.; Fletcher, C.H.; Barbee, M.; Anderson, T.R. The Influence of Seasonal Patterns on a Beach Nourishment Project in a Complex Reef Environment. *Coast. Eng.* **2016**, *116*, 67–76. [CrossRef]

8. Dolan, R.; Hayden, B.; Heywood, J. A New Photogrammetric Method for Determining Shoreline Erosion. *Coast. Eng.* **1978**, *2*, 21–39. [CrossRef]

9. Coyne, M.A.; Fletcher, C.H.; Richmond, B.M. Mapping Coastal Erosion Hazard Areas in Hawaii: Observations and Errors. *J. Coast. Res.* **1999**, 171–184. Available online: https://www.jstor.org/stable/25736194 (accessed on 1 August 2022).

10. Rooney, J.J.B.; Fletcher, C.H. A High Resolution, Digital, Aerial Photogrammetric Analysis of Historical Shoreline Change and Net Sediment Transport along the Kihei Coast of Maui, Hawaii. In Proceedings of the Thirteenth Annual National Conference on Beach Preservation Technology, Melbourne, FL, USA, 2–4 February 2000.

11. Genz, A.S.; Fletcher, C.H.; Dunn, R.A.; Frazer, L.N.; Rooney, J.J. The Predictive Accuracy of Shoreline Change Rate Methods and Alongshore Beach Variation on Maui, Hawaii. *J. Coast. Res.* **2007**, *23*, 87–105. [CrossRef]

12. Romine, B.M.; Fletcher, C.H. A Summary of Historical Shoreline Changes on Beaches of Kauai, Oahu, and Maui, Hawaii. *J. Coast. Res.* **2013**, *29*, 605–614. [CrossRef]

13. Rahman, A.A.A.; Awang, N.A.; Maulud, K.N.A.; Hamzah, M.L.; Selamat, S.N.; Mohd, F.A.; Zainal, M.K.; Wahid, M.A.A.; Ariffin, E.H. Multi Method Analysis for Identifying the Shoreline Erosion during Northeast Monsoon Season. *J. Sustain. Sci. Manag.* **2019**, *14*, 43–54.

14. Baig, M.R.I.; Ahmad, I.A.; Shahfahad;Tayyab, M.; Rahman, A. Analysis of Shoreline Changes in Vishakhapatnam Coastal Tract of Andhra Pradesh, India: An Application of Digital Shoreline Analysis System (DSAS). *Ann. GIS* **2020**, *26*, 361–376. [CrossRef]

15. Stockdon, H.F.; Sallenger, A.H.; List, J.H.; Holman, R.A. Estimation of Shoreline Position and Change Using Airborne Topographic Lidar Data. *J. Coast. Res.* **2002**, *18*, 502–513.

16. White, S.A.; Wang, Y. Utilizing DEMs Derived from LiDAR Data to Analyze Morphologic Change in the North Carolina Coastline. *Remote Sens. Environ.* **2003**, *85*, 39–47. [CrossRef]

17. Holman, R.A.; Stanley, J. The History and Technical Capabilities of Argus. *Coast. Eng.* **2007**, *54*, 477–491. [CrossRef]

18. Harley, M.D.; Turner, I.L.; Short, A.D.; Ranasinghe, R. Assessment and Integration of Conventional, RTK-GPS and Image-Derived Beach Survey Methods for Daily to Decadal Coastal Monitoring. *Coast. Eng.* **2011**, *58*, 194–205. [CrossRef]

19. Lomax, A.S.; Corso, W.; Etro, J.F. Employing Unmanned Aerial Vehicles (UAVs) as an Element of the Integrated Ocean Observing System. In Proceedings of the OCEANS 2005 MTS/IEEE, Washington, DC, USA, 17–23 September 2005; pp. 184–190. [CrossRef]

20. Delacourt, C.; Allemand, P.; Jaud, M.; Grandjean, P.; Deschamps, A.; Ammann, J.; Cuq, V.; Suanez, S. DRELIO: An Unmanned Helicopter for Imaging Coastal Areas. *J. Coast. Res.* **2009**, *6*, 1489–1493.

21. Beretta, F.; Shibata, H.; Cordova, R.; Peroni, R.D.L.; Azambuja, J.; Costa, J.F.C.L. Topographic Modelling Using UAVs Compared with Traditional Survey Methods in Mining. *REM-Int. Eng. J.* **2018**, *71*, 463–470. [CrossRef]

22. Mancini, F.; Dubbini, M.; Gattelli, M.; Stecchi, F.; Fabbri, S.; Gabbianelli, G. Using Unmanned Aerial Vehicles (UAV) for High-Resolution Reconstruction of Topography: The Structure from Motion Approach on Coastal Environments. *Remote Sens.* **2013**, *5*, 6880–6898. [CrossRef]

23. Casella, E.; Rovere, A.; Pedroncini, A.; Stark, C.P.; Casella, M.; Ferrari, M.; Firpo, M. Drones as Tools for Monitoring Beach Topography Changes in the Ligurian Sea (NW Mediterranean). *Geo-Mar. Lett.* **2016**, *36*, 151–163. [CrossRef]

24. Scarelli, F.M.; Sistilli, F.; Fabbri, S.; Cantelli, L.; Barboza, E.G.; Gabbianelli, G. Seasonal Dune and Beach Monitoring Using Photogrammetry from UAV Surveys to Apply in the ICZM on the Ravenna Coast (Emilia-Romagna, Italy). *Remote Sens. Appl. Soc. Environ.* **2017**, *7*, 27–39. [CrossRef]

25. Guisado-Pintado, E.; Jackson, D.W.T.; Rogers, D. 3D Mapping Efficacy of a Drone and Terrestrial Laser Scanner over a Temperate Beach-Dune Zone. *Geomorphology* **2019**, *328*, 157–172. [CrossRef]

26. Casella, E.; Drechsel, J.; Winter, C.; Benninghoff, M.; Rovere, A. Accuracy of Sand Beach Topography Surveying by Drones and Photogrammetry. *Geo-Mar. Lett.* **2020**, *40*, 255–268. [CrossRef]

27. Mikkelsen, A.B.; Anderson, T.R.; Coats, S.; Fletcher, C.H. Complex Drivers of Reef-Fronted Beach Change. *Mar. Geol.* **2022**, *446*, 106770. [CrossRef]

28. Dail, H.J.; Merrifield, M.A.; Bevis, M. Steep Beach Morphology Changes Due to Energetic Wave Forcing. *Mar. Geol.* **2000**, *162*, 443–458. [CrossRef]

29. Turner, I.L.; Harley, M.D.; Drummond, C.D. UAVs for Coastal Surveying. *Coast. Eng.* **2016**, *114*, 19–24. [CrossRef]

30. Hemmelder, S.; Marra, W.; Markies, H.; De Jong, S.M. Monitoring River Morphology & Bank Erosion Using UAV Imagery–A Case Study of the River Buëch, Hautes-Alpes, France. *Int. J. Appl. Earth Obs. Geoinf.* **2018**, *73*, 428–437.

31.　Betts, H.D.; Trustrum, N.A.; Rose, R.C.D. Geomorphic Changes in a Complex Gully System Measured from Sequential Digital Elevation Models, and Implications for Management. *Earth Surf. Process. Landf. J. Br. Geomorphol. Res. Group* **2003**, *28*, 1043–1058. [CrossRef]

32.　Baldi, P.; Fabris, M.; Marsella, M.; Monticelli, R. Monitoring the Morphological Evolution of the Sciara Del Fuoco during the 2002–2003 Stromboli Eruption Using Multi-Temporal Photogrammetry. *ISPRS J. Photogramm. Remote Sens.* **2005**, *59*, 199–211. [CrossRef]

33.　Pesci, A.; Fabris, M.; Conforti, D.; Loddo, F.; Baldi, P.; Anzidei, M. Integration of Ground-Based Laser Scanner and Aerial Digital Photogrammetry for Topographic Modelling of Vesuvio Volcano. *J. Volcanol. Geotherm. Res.* **2007**, *162*, 123–138. [CrossRef]

34.　Paul, F.; Haeberli, W. Spatial Variability of Glacier Elevation Changes in the Swiss Alps Obtained from Two Digital Elevation Models. Geophys. *Res. Lett.* **2008**, *35*, L21502. [CrossRef]

35.　Wendt, A.; Mayer, C.; Lambrecht, A.; Floricioiu, D. A Glacier Surge of Bivachny Glacier, Pamir Mountains, Observed by a Time Series of High-Resolution Digital Elevation Models and Glacier Velocities. *Remote Sens.* **2017**, *9*, 388. [CrossRef]

36.　Berthier, E.; Cabot, V.; Vincent, C.; Six, D. Decadal Region-Wide and Glacier-Wide Mass Balances Derived from Multi-Temporal ASTER Satellite Digital Elevation Models. Validation over the Mont-Blanc Area. *Front. Earth Sci.* **2016**, *4*, 63. [CrossRef]

37.　Berthier, E.; Toutin, T. SPOT5-HRS Digital Elevation Models and the Monitoring of Glacier Elevation Changes in North-West Canada and South-East Alaska. *Remote Sens. Environ.* **2008**, *112*, 2443–2454. [CrossRef]

38.　Ge, L.; Chang, H.-C.; Rizos, C. Mine Subsidence Monitoring Using Multi-Source Satellite SAR Images. *Photogramm. Eng. Remote Sens.* **2007**, *73*, 259–266. [CrossRef]

39.　Carabassa, V.; Montero, P.; Crespo, M.; Padró, J.-C.; Pons, X.; Balagué, J.; Brotons, L.; Alcañiz, J.M. Unmanned Aerial System Protocol for Quarry Restoration and Mineral Extraction Monitoring. *J. Environ. Manag.* **2020**, *270*, 110717. [CrossRef]

40.　Padró, J.-C.; Cardozo, J.; Montero, P.; Ruiz-Carulla, R.; Alcañiz, J.M.; Serra, D.; Carabassa, V. Drone-Based Identification of Erosive Processes in Open-Pit Mining Restored Areas. *Land* **2022**, *11*, 212. [CrossRef]

41.　Davis, J.M.; Grindrod, P.M.; Boazman, S.J.; Vermeesch, P.; Baird, T. Quantified Aeolian Dune Changes on Mars Derived from Repeat Context Camera Images. *Earth Space Sci.* **2020**, *7*, e2019EA000874. [CrossRef]

42.　Qin, R.; Tian, J.; Reinartz, P. 3D Change Detection–Approaches and Applications. *ISPRS J. Photogramm. Remote Sens.* **2016**, *122*, 41–56. [CrossRef]

43.　James, L.A.; Hodgson, M.E.; Ghoshal, S.; Latiolais, M.M. Geomorphic Change Detection Using Historic Maps and DEM Differencing: The Temporal Dimension of Geospatial Analysis. *Geomorphology* **2012**, *137*, 181–198. [CrossRef]

44.　Sea Engineering, Inc. *Final Environmental Assessment Waikiki Beach Maintenance, Prepared for State of Hawaii Department of Land and Natural Resources*; Makai Research Pier: Waimanalo, HI, USA, 2010.

45.　State of Hawaii Department of Land and Natural Resources Office of Conservation and Coastal Lands 2021 Waikīkī Beach Maintenance Project. Available online: https://dlnr.hawaii.gov/occl/waikiki/ (accessed on 29 April 2022).

46.　Clark, J.R.K. *Beaches of O'ahu*, Revised Edition; University of Hawai'i Press: Honolulu, HI, USA, 2005.

47.　Gerritsen, F. *Beach and Surf Parameters in Hawai'i*; University of Hawaii, Sea Grant College Program: Honolulu, HI, USA, 1978; Volume 78.

48.　Homer, P.S. Characteristics of Deep Water Waves in O'ahu Area for a Typical Year. In *Prepared for the Board of Harbor Commissioners, State of Hawaii*; Contract No. 5772; Marine Advisors: La Jolla, CA, USA, 1964.

49.　Vitousek, S.; Fletcher, C.H. Maximum Annually Recurring Wave Heights in Hawai'i. *Pac. Sci.* **2008**, *62*, 541–553. [CrossRef]

50.　Moberly, R.M.; Chamberlain, T. *Hawaiian Beach Systems*; Final Report HIG-64-2; Hawaii Institute of Geophysics, University of Hawaii: Honolulu, HI, USA, 1964.

51.　Simpson, R.H. Evolution of the Kona Storm a Subtropical Cyclone. *J. Atmospheric Sci.* **1952**, *9*, 24–35. [CrossRef]

52.　Murakami, H.; Wang, B.; Li, T.; Kitoh, A. Projected Increase in Tropical Cyclones near Hawaii. *Nat. Clim. Change* **2013**, *3*, 749–754. [CrossRef]

53.　National Oceanic and Atmospheric Administration (NOAA) Tropical Cyclones—Annual 2018 | National Centers for Environmental Information (NCEI). Available online: https://www.ncei.noaa.gov/access/monitoring/monthly-report/tropical-cyclones/201813#pac (accessed on 16 May 2019).

54.　Berg, R.; Houston, S.; Birchard, T. National Hurricane Center/Central Pacific Hurricane Center Tropical Cyclone Report—Hurricane Hector (EP102018). 2019. Available online: https://www.nhc.noaa.gov/data/tcr/EP102018_Hector.pdf (accessed on 1 August 2022).

55.　Beven, J.L., II; Wroe, D. National Hurricane Center/Central Pacific Hurricane Center Tropical Cyclone Report—Hurricane Lane (EP142018). 2019. Available online: https://www.nhc.noaa.gov/data/tcr/EP142018_Lane.pdf (accessed on 1 August 2022).

56.　Cangialosi, J.P.; Jelsema, J. National Hurricane Center/Central Pacific Hurricane Center Tropical Cyclone Report—Hurricane Olivia (EP172018). 2019. Available online: https://www.nhc.noaa.gov/data/tcr/EP172018_Olivia.pdf (accessed on 1 August 2022).

57.　Houston, S.; Birchard, T. Central Pacific Hurricane Center Tropical Cyclone Report—Hurricane Walaka (CP012018). 2020. Available online: https://www.nhc.noaa.gov/data/tcr/CP012018_Walaka.pdf (accessed on 1 August 2022).

58.　Knapp, K.R.; Kruk, M.C.; Levinson, D.H.; Diamond, H.J.; Neumann, C.J. The International Best Track Archive for Climate Stewardship (IBTrACS): Unifying Tropical Cyclone Best Track Data. *Bull. Am. Meteorol. Soc.* **2010**, *91*, 363–376. [CrossRef]

59. Knapp, K.R.; Diamond, H.J.; Kossin, J.P.; Kruk, M.C.; Schreck, C.J. *International Best Track Archive for Climate Stewardship (IBTrACS) Project, Version 4*; Eastern Pacific Basin; NOAA National Centers for Environmental Information: Asheville, NC, USA, 2018. Available online: https://www.ncei.noaa.gov/products/international-best-track-archive (accessed on 21 October 2021).

60. Norcross, Z.M.; Fletcher, C.H.; Rooney, J.J.B.; Eversole, D.; Miller, T.L. Hawaiian Beaches Dominated by Longshore Transport. *Coast. Sediments* **2003**, *3*, 1–15.

61. Vautherin, J.; Rutishauser, S.; Schneider-Zapp, K.; Choi, H.F.; Chovancova, V.; Glass, A.; Strecha, C.; Sa, D. Photogrammetric Accuracy and Modeling of Rolling Shutter Cameras. *ISPRS J. Photogramm. Remote Sens.* **2016**, *3*, 139–146. [CrossRef]

62. Datums—NOAA Tides & Currents. Available online: https://tidesandcurrents.noaa.gov/datums.html?datum=MSL&units=1&epoch=0&id=1612340&name=Honolulu&state=HI (accessed on 18 April 2022).

63. Over, J.-S.R.; Ritchie, A.C.; Kranenburg, C.J.; Brown, J.A.; Buscombe, D.D.; Noble, T.; Sherwood, C.R.; Warrick, J.A.; Wernette, P.A. *Processing Coastal Imagery with Agisoft Metashape Professional Edition, Version 1.6—Structure from Motion Workflow Documentation*; Open-File Report; U.S. Geological Survey: Reston, VA, USA, 2021. [CrossRef]

64. Fletcher, C.H. University of Hawaii Sea Grant College Program (UHSG) Mean Higher High Water (MHHW) Sea Level: Honolulu, Hawaii. Distributed by the Pacific Islands Ocean Observing System (PacIOOS). 2014. Available online: https://www.pacioos.hawaii.edu/metadata/hi_csp_hono_mhhw.html (accessed on 13 November 2018).

65. Winant, C.D.; Inman, D.L.; Nordstrom, C.E. Description of Seasonal Beach Changes Using Empirical Eigenfunctions. *J. Geophys. Res.* **1975**, *80*, 1979–1986. [CrossRef]

66. Aubrey, D.G. Seasonal Patterns of Onshore/Offshore Sediment Movement. *J. Geophys. Res. Ocean.* **1979**, *84*, 6347–6354. [CrossRef]

67. Dick, J.E.; Dalrymple, R.A. Coastal Changes at Bethany Beach, Delaware. *Coast. Eng. Proc.* **1984**, *1*, 112. [CrossRef]

68. Losada, M.A.; Medina, R.; Vidal, C.; Roldán, A. Historical Evolution and Morphological Analysis of "El Puntal" Spit, Santander (Spain). *J. Coast. Res.* **1991**, *7*, 711–722.

69. Anderson, T.R.; Neil Frazer, L.; Fletcher, C.H. Transient and Persistent Shoreline Change from a Storm. *Geophys. Res. Lett.* **2010**, *37*. [CrossRef]

70. Cheung, K.F. Simulating WAves Nearshore (SWAN) Regional Wave Model: Oahu. April–December 2018 Distributed Pacific Islands Ocean Observing System (PacIOOS). Available online: https://www.pacioos.hawaii.edu/metadata/swan_oahu.html (accessed on 18 February 2019).

71. McManus, M.A.; Merrifield, M.A. Pacific Islands Ocean Observing System (PacIOOS) PacIOOS Wave Buoy 098: Mokapu Point, Oahu, Hawaii. January 2018–February 2020. Wave Energy Flux (South Swell). Distributed by the Coastal Data Information Program (CDIP). 2000. Available online: http://www.pacioos.hawaii.edu/metadata/cdip098.html?format=fgdc (accessed on 23 March 2020).

72. McManus, M.A.; Merrifield, M.A. Pacific Islands Ocean Observing System (PacIOOS) PacIOOS Wave Buoy 233: Pearl Harbor Entrance, Oahu, Hawaii January 2018–February 2020. Wave Energy Flux (Trade-Wind Waves). Distributed by the Coastal Data Information Program (CDIP). 2017. Available online: https://www.pacioos.hawaii.edu/metadata/cdip233.html (accessed on 23 March 2020).

73. Dean, R.G.; Dalrymple, R.A. *Coastal Processes with Engineering Applications*; Cambridge University Press: Cambridge, UK, 2004.